Journal of Engineering Mathematics **47:** 387–404, 2003.

Blood flow in the human ascending aorta: a combined MRI and CFD study

ARMIN LEUPRECHT[1], SEBASTIAN KOZERKE[2], PETER BOESIGER[2] and KARL PERKTOLD[1]
[1]*Institute of Mathematics, Graz University of Technology, Graz, Austria (e-mail: armin.leuprecht@tugraz.at);*
[2]*Institute of Biomedical Engineering, University of Zurich and Swiss Federal Institute of Technology Zurich, Zurich, Switzerland*

Received 31 October 2002; accepted in revised form 14 August 2003

Abstract. Blood flow through the ascending aorta of two individuals is studied numerically. Realistic flow simulation is enabled by the combination of MRI and CFD. The aim of this study is the validation of the calculated flow field and, on the other hand, a comparison between flow distal to an artificial heart valve and native flow of a healthy volunteer. Three-dimensional, time-dependent computer models of the human ascending aorta were reconstructed from three-directional data sets acquired by MRI in the subjects studied. MRI velocity measurements downstream of the aortic valve provided the inflow conditions for the computational study. The pulsatile flow is described by the ALE-modified Navier-Stokes equations with respect to the time-varying flow domain. The numerical approach applies our own developed finite-element solver. During systolic acceleration the flow patterns distal to the valves do not show major differences between the two configurations. During flow deceleration, however, a significant influence of the disturbed inflow conditions can be found in the whole segment. Using the methods proposed, simulation of blood flow in the ascending aorta of the two subjects could be successfully performed. There was good qualitative agreement of blood velocities predicted by CFD and velocity data measured by MRI. In conclusion, the approach described herein might offer a new way towards an improved assessment of detailed *in vivo* flow conditions and alterations of blood flow associated with heart valve prostheses in particular. Combining CFD and MRI potentially extends the quantification of hemodynamic variables *in vivo* at a scale beyond the resolution limit inherent to MRI.

Key words: arbitrary Lagrangian-eulerian method, artificial valve, finite element method, realistic modeling, wall shear stress

1. Introduction

The aorta is the main blood vessel transporting blood from the left heart to the systemic circulation. It is of complex three-dimensional geometry including curving, branching and tapering. Three planes of curvature exist with the aortic arch being the main bending of the vessel. At the sinuses distal to the aortic valve the coronary arteries, which provide the blood supply to the myocardium, are connected and at the top of the aortic arch three major arterial branches are present. The taper of the aorta is about fifty percent of the cross-sectional area reduction from the aortic root to the beginning of the descending aorta [1].

Blood flow in the ascending aorta exhibits complex patterns. During systole blood is accelerated, leaving the left ventricle through the aortic valve. Using hot-film anemometry measurements, it was shown by [2] that velocity profiles distal to the valve are essentially flat in the ascending aorta and skewed towards the inner wall with respect to the aortic arch. Reversed flow at the inner wall has also been reported during systolic deceleration and

the diastolic phase. Large regions of the vessel walls are exposed to high and/or low shear stress. Such regions are known to be preferred locations for the genesis and development of atherosclerotic lesions [3]. Numerous experimental studies, as well as numerical investigations on the aortic flow dynamics, have been performed. Studies in idealized geometries [4, 5] have yielded a basic understanding of occurring flow phenomena. Since local flow is strongly affected by geometry, more detailed models of *in vivo* anatomy have become necessary [6–8]. An important step towards realistic flow simulations concerns the generation of appropriate computational models. Recent advances in magnetic-resonance-imaging (MRI) technology have made this modality a method of choice for assessing morphological and functional information of the cardio-vascular system. This non-invasive technique allows the measurement of complex arterial geometries including their movement, as well as blood velocities throughout the cardiac cycle [9, 10]. In this way MRI can provide the anatomical and hemodynamic input for the computational-fluid-dynamic (CFD) simulations that provide an opportunity for obtaining a full set of hemodynamic data. The prediction of important hemodynamic quantities, such as wall shear stress, that cannot be measured directly in the human vascular system is enabled by a combination of these two methods. An important point in the combination of computer simulation and measurement is the validation of the results [11, 12]. In the present study MRI and CFD results for axial and secondary flow patterns have been compared. Combining CFD and MRI might hold promise for a number of applications in the cardio-vascular system. In particular, investigation of blood-flow alterations associated with cardio-vascular implants appears promising. In a first attempt, blood flow downstream of an artificial aortic valve implanted in a patient is studied by means of realistic simulations and compared to blood-flow characteristics in the ascending aorta of a healthy volunteer.

Clinically important late complications have been reported in patients with mechanical valve prostheses. Some of these problems have been associated with differences in the hemodynamic performance of artificial valves with respect to native valves [13–15]. Nevertheless mechanical heart valves are preferred over other replacement valves for subjects with a life expectancy greater than ten years due to the long-term durability of the mechanical implants.

The mathematical description of the aortic blood flow uses the time dependent, three-dimensional, incompressible Navier-Stokes equations for Newtonian fluids. The movement of the vessel segment during the cardiac cycle caused by the motion of the heart is to be addressed. This is done by the application of the arbitrary Lagrangian-Eulerian (ALE) method. This method has proven to be a powerful tool for the description of flow through moving domains and has been studied by many authors (*e.g.* [16–18]). The numerical solution method applies a velocity-pressure correction technique for finite elements.

2. Methods

2.1. MRI DATA ACQUISITION

Due to its superior spatial resolution and image contrast compared with Doppler ultrasound MR velocity mapping has proven the method of choice for the non-invasive quantification of velocity fields around heart valves *in vivo.*

MR velocity mapping is based on the detection of the acquired phase shift of proton spins moving along a magnetic-field gradient. Velocity encoding is incorporated by adding two gradients lobes of equal duration and opposite amplitudes to a standard MR imaging sequence. Thereby a linear relation between the phase shift in each voxel and the velocity

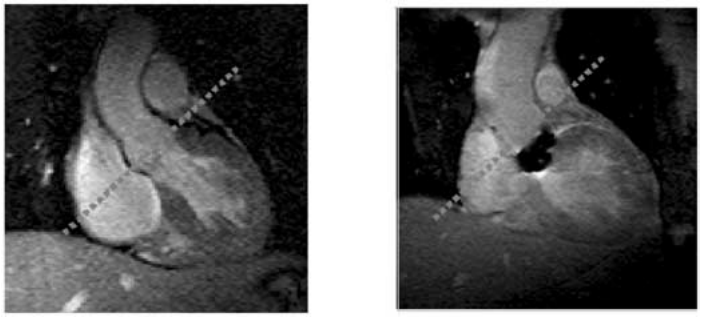

Figure 1. Velocity measurement slice: native configuration (left) and artificial heart (right).

of motion encoded along the added bipolar gradient is established. Due to magnetic-field inhomogeneities and susceptibility variations within the patient, it is necessary to perform two acquisitions with different velocity encoding. The subtraction of the phase images from the two acquisitions yields the final velocity map, resolving spatial distributions of velocities in addition to morphological information.

In the *in vivo* situation, measurements may be compromised by the active cyclic motion of the heart (cardiac contraction and dilation) and the passive motion of the heart due to respiration. These motion components may lead to image artifacts and uncertainties about the exact measurement site with respect to heart valves.

2.1.1. *Respiratory-motion compensation*

To compensate for the passive motion of the heart resulting from respiration, two-dimensional spatially selective excitation pulses (navigators) were implemented to detect the actual breathing state on the diaphragm of the patient [19]. Navigators were used at the beginning and at the end of each heart beat. Only if the breathing state was within a predefined window data was accepted for reconstruction.

2.1.2. *Cardiac-motion compensation*

Adaptation of the actual slice position to the active motion of the heart was achieved using a recently proposed moving slice imaging technique [20]. In essence, a subtractive labeling technique is used to mark and trace points labeled on the basal plane of the heart, thus allowing assessment of through-plane motion of any of the cardiac valves throughout the cardiac cycle.

For moving-slice-velocity mapping a gradient echo phase contrast sequence interleaving the two velocity encoding segments was adapted. In-plane resolution was 1×1 mm^2 and imaging slice thickness amounted to 5 mm. Velocity data was recorded in intervals of 30 ms throughout the cardiac cycle starting 62 ms after the R-wave of the ECG. The initial delay after R-wave detection was required for execution of the navigator pulse and processing of the navigator signal. Velocity in slice selecting direction was encoded with an encoding velocity of 150 cm/s. To reduce intra-voxel dephasing effects in complex flow fields, only 75% of the full echo was acquired yielding an echo time of 3·9 ms. Missing samples were zero padded and an asymmetric weighting function was applied to the central portion of the spatial frequency domain of the data before Fourier transform. Accounting for an average gating efficiency of about 75% and a heart rate of 70 beats/min, scan duration was 3:30 minutes. Measurements were obtained at a distance of 1/4 valve diameter downstream from the aortic valve (Figure 1).

2.1.3. *Experimental setup*
A healthy, female subject and a patient who had a St. Jude Medical aortic valve implanted underwent MR examinations. Written informed consent was obtained from both subjects. The study was approved by the local Ethics Committee and complied with the Helsinki II declaration. Measurements were carried out using a Philips Gyroscan NT 1.5T whole body scanner (Philips Medical Systems, Best, The Netherlands) with the subjects lying in supine position inside the scanner bore.

2.1.4. *Geometric model*
Aortic geometry was reconstructed from contours extracted on ten axial slices of the ascending aorta acquired at increasing distances from the aortic valve in the healthy subject. A dedicated procedure was used to remove discontinuities of the extracted contours over space and time. The aortic geometry was then matched to the single-slice cross-sectional data obtained in the patient.

3. Mathematical model

3.1. Computational model

The extracted geometric data consists of ten cross-sections given by 24 points each for 35 time steps over the entire cardiac cycle. In order to model the beginning of the aortic arch and to reduce the influence of the outflow boundary conditions the vessel segment was extended downstream by about one inflow diameter using a Bezier curve for the axial line. A bi-cubic spline algorithm was developed to create an accurate and smooth model of the inner-vessel wall surface (Figure 2). The procedure applies smoothing of the axis-line and the surface in space and periodically in time. The three-dimensional computational mesh is generated for all computational time steps. The volume-filling method starts from a specified 3D grid distribution in a straight cylindrical tube using the same surface-mesh structure as the vessel models. In the first step the tube (occupying $\Omega \in \mathbb{R}^3$) is mapped to the aorta model by the solution of the Laplacian equation with the known wall deformations $\boldsymbol{f}$ as Dirichlet boundary condition

$$\begin{aligned} \Delta \boldsymbol{d} &= 0 \qquad \text{in } \Omega, \\ \boldsymbol{d} &= \boldsymbol{f} \qquad \text{on } \partial\Omega, \end{aligned} \tag{1}$$

where $\boldsymbol{d}$ denotes the field of the deformation between the cylindrical tube and the aorta model. Subsequently the finite-element mesh is generated for all computational time steps by successive application of the Laplacian solver.

Each component of the measured velocity data was smoothed over the cross-section at the computational inlet of the vessel segment. The procedure uses a NAG (The Numerical Algorithms Group Ltd, Oxford, UK) routine that is based on a surface-fitting algorithm of scattered data [21, Chapter 9]. It determines a smooth bi-cubic spline approximation $s(x, y)$ to a set of data points (x_i, y_i, f_i) with weights $w_i, i = 1, \ldots, m$. A single parameter S must be specified that controls the trade-off between the closeness of fit and the smoothness of fit. Recommended values for S are given in the literature [22] provided that the statistical error in f_i is known. Based on *in vitro* experiments, a standard deviation of 4% was indicated. However, due to the heart motion, this value cannot be applied to the *in vivo* data. Therefore all weights had to be set to one and S was determined by trial and error. Too small values of

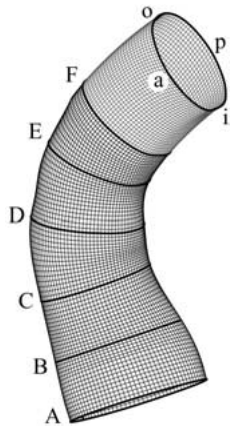

Figure 2. Computational model of the ascending aorta (healthy configuration); a (anterior wall), i (inner wall), p (posterior wall) and 0 (outer wall); A – F denote locations of planes where computed results are demonstrated.

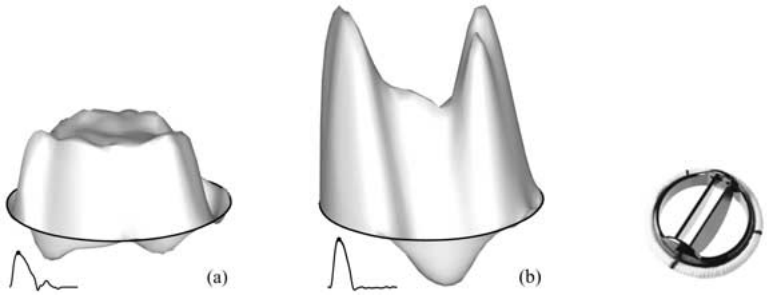

Figure 3. Axial inflow velocity profiles at peak flow and corresponding flow pulse wave form: Native configuration (a) and artificial heart valve (b). Right: St. Jude Medical® mechanical valve.

S result in spurious oscillations, whereas too large values lead to the loss of the signal and the spline will be too smooth. Reasonable values were examined by graphical analysis and were in the range between 500 and 2000. On successful completion the weighted sum of squared residuals equals the smoothing parameter S

$$\sum_{i=1}^{m} \epsilon_i^2 = S, \qquad \epsilon_i = w_i(f_i - s(x_i, y_i)), \qquad i = 1, \ldots, m \tag{2}$$

The knots of the spline were located automatically by the routine on the rectangle $[x_{\min}, x_{\max}] \times [y_{\min}, y_{\max}]$. Numerical experiments revealed the necessity of putting sampling points of zero velocity and higher weights outside the vessel cross-section within the rectangle. After the smoothing procedure, the velocity profiles were interpolated to all time steps on the time-dependent finite-element mesh of the entrance slice and scaled to the correct flow rate. Figure 3 shows the profiles at systolic peak flow for the native configuration and the artificial valve configuration distal to the St. Jude Medical mechanical valve. These profiles were used as inflow boundary conditions in the numerical computations. In the healthy subject, velocity data was also available at the entrance of the aortic arch and was used for validation purposes. Data was treated according to the procedures described for the profiles imposing inflow boundary conditions.

3.2. FLOW MODEL AND BOUNDARY CONDITIONS

The classical approach to the solution of flow problems uses the Eulerian viewpoint (where the observer is fixed) because of its capability to handle large deformations. When dealing with moving flow domains, however, great effort is required to describe the boundary and convective effects that occur due to a relative movement between the material point and the observer. The application of the arbitrary Lagrangian Eulerian (ALE) technique addresses these difficulties. Early presentations of the method can be found for example in [16] and [23]. A detailed description is given in [24].

At time $t \geq t_0$ the continuum occupies the region $\Omega_t \in I\!R^3$ that varies with time. Let Ω_0 denote the region at the initial time $t = t_0$. The family of mappings

$$\Phi_t : \Omega_0 \subset I\!R^3 \to \Omega_t \subset I\!R^3, \qquad \boldsymbol{y}(\boldsymbol{x}, t) = \Phi_t(\boldsymbol{x}) \tag{3}$$

associates a point $\boldsymbol{x}$ of the reference configuration Ω_0 (ALE frame) to a point $\boldsymbol{y}$ on the current domain configuration Ω_t (spatial or Eulerian frame) for each $t \in (t_0, T)$. Furthermore Φ_t is assumed to be a homeomorphism, *i.e.*, $\Phi_t \in C_0(\overline{\Omega_0})$ and it is invertible with a continuous inverse $\Phi_t^{-1} \in C_0(\overline{\Omega_t})$.

Considering a vector-valued function $\boldsymbol{u} : \Omega_t \times (0, T) \to I\!R^3$ defined on the Eulerian frame the corresponding function $\boldsymbol{u}^* := \boldsymbol{u} \circ \Phi_t$ on the ALE frame is defined as

$$\boldsymbol{u}^* : \Omega_0 \times (0, T) \to I\!R^3, \qquad \boldsymbol{u}^*(\boldsymbol{x}, t) = \boldsymbol{u}(\Phi_t(\boldsymbol{x}), t). \tag{4}$$

The time derivative of the function $\boldsymbol{u}$ in the ALE frame written in spatial coordinates is given by applying the chain rule

$$\left.\frac{\partial \boldsymbol{u}}{\partial t}\right|_x (\boldsymbol{y}, t) = \left.\frac{\partial \boldsymbol{u}}{\partial t}\right|_y (\boldsymbol{y}, t) + \left(\left.\frac{\partial \boldsymbol{y}}{\partial t}\right|_x \cdot \nabla_y\right) \boldsymbol{u}(\boldsymbol{y}, t). \tag{5}$$

The symbol ∇_y indicates the space derivative with respect to the Eulerian coordinates. The time derivative of the spatial coordinate $\boldsymbol{y}$ expressed in ALE coordinates corresponds to the domain velocity and will be referred to by

$$\hat{\boldsymbol{u}}(\boldsymbol{y}, t) = \left.\frac{\partial \boldsymbol{y}}{\partial t}\right|_x . \tag{6}$$

It is now possible to recast the Navier-Stokes equations (where the body forces are neglected) that are used to describe the pulsatile blood flow on the time-varying domain Ω_t

$$\rho \left(\left.\frac{\partial \boldsymbol{u}}{\partial t}\right|_y + (\boldsymbol{u} \cdot \nabla)\boldsymbol{u} \right) = \nabla \cdot \boldsymbol{\sigma}, \tag{7}$$

$$\nabla \cdot \boldsymbol{u} = 0, \tag{8}$$

from the Eulerian frame to the ALE frame

$$\rho \left(\left.\frac{\partial \boldsymbol{u}}{\partial t}\right|_x - (\hat{\boldsymbol{u}} \cdot \nabla)\boldsymbol{u} + (\boldsymbol{u} \cdot \nabla)\boldsymbol{u} \right) = \nabla \cdot \boldsymbol{\sigma}, \tag{9}$$

$$\nabla \cdot \boldsymbol{u} = 0, \tag{10}$$

where $\boldsymbol{u}$ is the fluid velocity, $\hat{\boldsymbol{u}}$ denotes the domain velocity, $\boldsymbol{\sigma}$ is the Cauchy stress tensor and ρ is the constant fluid density. In the following we will use $\boldsymbol{c} = \boldsymbol{u} - \hat{\boldsymbol{u}}$ to denote the convective

velocity which is the difference of the fluid velocity and the domain velocity. As all space derivatives are taken in the Eulerian frame, we will omit the indicating index ($\nabla \equiv \nabla_y$).

In this study blood is assumed to be Newtonian. Therefore the symmetric stress tensor can be expressed by the constitutive equation

$$\boldsymbol{\sigma} = -p\boldsymbol{I} + 2\mu\boldsymbol{\epsilon}(\boldsymbol{u}), \tag{11}$$

where p is the fluid pressure, $\boldsymbol{I}$ is the unit tensor, μ denotes the apparent fluid viscosity and $\boldsymbol{\epsilon}(\boldsymbol{u})$ is the rate-of-strain tensor defined as

$$\boldsymbol{\epsilon}(\boldsymbol{u}) = \frac{1}{2}\left(\nabla\boldsymbol{u} + \nabla\boldsymbol{u}^T\right). \tag{12}$$

With respect to the incompressible mass conservation, the extra-stresses can be conveniently inserted into the equation of motion leading to a closed form of the Navier-Stokes system. When the reference length L_0, the reference velocity U_0 and the kinematic viscosity $\nu = \mu/\rho$ are introduced, the equations can be written in non-dimensional form

$$\left.\frac{\partial\boldsymbol{u}}{\partial t}\right|_x + (\boldsymbol{c}\cdot\nabla)\boldsymbol{u} - \frac{1}{\mathrm{Re}}\Delta\boldsymbol{u} + \nabla p = 0, \tag{13}$$

$$\nabla\cdot\boldsymbol{u} = 0, \tag{14}$$

where $\mathrm{Re} = U_0L_0/\nu$ is the Reynolds number.

The boundary of the time-varying flow domain Ω_t consists of two disjunct sections $\Gamma_t = \Gamma_u \cup \Gamma_s$, $\Gamma_u \cap \Gamma_s = \emptyset$. At the inlet and the vessel wall the time-dependent velocities are prescribed.

$$\boldsymbol{u}(t) = \boldsymbol{g}(t), \qquad t > 0, \quad \text{on } \Gamma_u. \tag{15}$$

The three-directional velocity distribution measured by MRI is used as inflow boundary condition. At the vessel walls the no-slip condition is imposed, *i.e.*, the velocity is gained from the MRI geometry measurements. At the outflow boundary the surface traction force is prescribed which is mathematically modeled by the Neumann boundary condition

$$\boldsymbol{\sigma}\cdot\boldsymbol{n} = \boldsymbol{h}(t), \qquad t > 0, \quad \text{on } \Gamma_s, \tag{16}$$

where $\boldsymbol{n}$ denotes the outward-pointing normal unit vector. The specification of appropriate force conditions at the artificial boundary is a difficult task in general. In this study the computational domain was extended by about one inflow diameter in order to minimize the influence of the applied idealized traction free outflow ($\boldsymbol{h} = 0$) on the flow region of interest.

The necessity of appropriate initial conditions is superseded by the periodicity property of the pulsatile flow.

4. Numerical approach

The Navier-Stokes equations are solved numerically by means of a finite-element method. A weak form of the Navier-Stokes equations (13) and (14) in the ALE formulation may be

formally written as

$$\int_{\Omega_t} \left.\frac{\partial \boldsymbol{u}}{\partial t}\right|_x \cdot \boldsymbol{v}\,\mathrm{d}\Omega + \int_{\Omega_t} (\boldsymbol{c}\cdot\nabla\boldsymbol{u})\cdot\boldsymbol{v}\,\mathrm{d}\Omega + \frac{1}{\mathrm{Re}}\int_{\Omega_t} \nabla\boldsymbol{u} : \nabla\boldsymbol{v}\,\mathrm{d}\Omega - \int_{\Omega_t} p\nabla\cdot\boldsymbol{v}\,\mathrm{d}\Omega = - \int_{\Gamma_t} p\boldsymbol{n}\cdot\boldsymbol{v}\,\mathrm{d}\Gamma + \frac{1}{\mathrm{Re}}\int_{\Gamma_t} (\nabla\boldsymbol{u}\cdot\boldsymbol{n})\cdot\boldsymbol{v}\,\mathrm{d}\Gamma, \qquad \forall \boldsymbol{v}\in\mathcal{V}(\Omega_t), \tag{17}$$

$$\int_{\Omega_t} \nabla\cdot\boldsymbol{u}q\,\mathrm{d}\Omega = 0, \qquad \forall q\in\mathcal{Q}(\Omega_t), \tag{18}$$

where $\boldsymbol{u}$ and p are sought in appropriate functional spaces. The boundary integral on the right-hand side of expression (17) reduces to the outflow section as the test functions $\boldsymbol{v}$ vanish on the moving Dirichlet boundary Γ_u. Therefore, it represents the stresses on Γ_s taken into account the incompressibility of the fluid

$$\int_{\Gamma_t} (-p\boldsymbol{n} + \frac{1}{\mathrm{Re}}\nabla\boldsymbol{u}\cdot\boldsymbol{n})\cdot\boldsymbol{v}\,\mathrm{d}\Gamma = \int_{\Gamma_s} \boldsymbol{h}\cdot\boldsymbol{v}\,\mathrm{d}\Gamma = 0 \tag{19}$$

and vanishes completely because a zero traction force is applied in this study ($\boldsymbol{h} = 0$). A stability analysis of the formulation has been performed in [25].

Formulation (17) is useful since the time derivative is taken in the fixed reference frame. To avoid time-dependent test functions (they must vanish on Γ_u, *i. e.*, the part of the moving boundary where essential boundary conditions are applied), a space of test functions $\mathcal{W}(\Omega_0) \equiv \boldsymbol{H}_0^1(\Omega_0)$ is introduced on the ALE frame Ω_0 that is made of smooth functions $\hat{\boldsymbol{v}} : \Omega_0 \to I\!R$. By means of the ALE mapping Φ_t the corresponding space of weighting functions on the Eulerian frame is obtained

$$\mathcal{V}(\Omega_t) = \left\{\boldsymbol{v} : \Omega_t \times (0,T) \to I\!R^3 : \boldsymbol{v} = \hat{\boldsymbol{v}}\circ\Phi_t^{-1}, \hat{\boldsymbol{v}}\in\mathcal{W}(\Omega_0)\right\}. \tag{20}$$

The space of pressure test functions is made of square-integrable functions over the domain Ω_t

$$\mathcal{Q}(\Omega_t) = \left\{q\in L^2(\Omega_t)\right\}. \tag{21}$$

In Equation (17) a time differentiation occurs under the integral that is taken over the varying volume Ω_t and, therefore, the two operations cannot be interchanged. This problem can be solved with help of the Reynolds transport theorem [26, Chapter 4], [27, pp. 210–211] that expresses the material time derivative of a physical measure that is given as a volume integral of a function $f : \Omega_t \times (0,T) \to I\!R$ in a moving domain

$$\frac{\mathrm{d}}{\mathrm{d}t}\int_{\Omega_t} f(\boldsymbol{y},t)\,\mathrm{d}\Omega = \int_{\Omega_t} \left\{ \left.\frac{\partial f}{\partial t}\right|_y + \nabla\cdot(f\hat{\boldsymbol{u}})\right\}(\boldsymbol{y},t)\,\mathrm{d}\Omega. \tag{22}$$

When the components of a vector field $\boldsymbol{u} = (u_1, u_2, u_3)$ are associated with the function f, the transport theorem can be written for vector-valued functions

$$\frac{\mathrm{d}}{\mathrm{d}t}\int_{\Omega_t} \boldsymbol{u}(\boldsymbol{y},t)\,\mathrm{d}\Omega = \int_{\Omega_t} \left\{ \left.\frac{\partial \boldsymbol{u}}{\partial t}\right|_y + \nabla\cdot(\hat{\boldsymbol{u}}\otimes\boldsymbol{u})\right\}(\boldsymbol{y},t)\,\mathrm{d}\Omega, \tag{23}$$

where the divergence of the tensor product is given by

$$\nabla \cdot (\hat{\boldsymbol{u}} \otimes \boldsymbol{u}) = \hat{\boldsymbol{u}} \cdot \nabla \boldsymbol{u} + \boldsymbol{u}(\nabla \cdot \hat{\boldsymbol{u}}). \tag{24}$$

Now, as the test functions in $\mathcal{V}(\Omega_t)$ do not depend on time, the following useful relations can be derived

$$\mathbf{0} = \left.\frac{\partial \boldsymbol{v}}{\partial t}\right|_x = \left.\frac{\partial \boldsymbol{v}}{\partial t}\right|_y + (\hat{\boldsymbol{u}} \cdot \nabla) v \quad \forall v \in \mathcal{V}(\Omega_t), \tag{25}$$

$$\frac{\mathrm{d}}{\mathrm{d}t}\int_{\Omega_t} \boldsymbol{v}\mathrm{d}\Omega = \int_{\Omega_t} \boldsymbol{v}\nabla \cdot \hat{\boldsymbol{u}}\mathrm{d}\Omega, \tag{26}$$

$$\frac{\mathrm{d}}{\mathrm{d}t}\int_{\Omega_t} \boldsymbol{v} \cdot \boldsymbol{u}\mathrm{d}\Omega = \int_{\Omega_t} \boldsymbol{v} \cdot \left(\left.\frac{\partial \boldsymbol{u}}{\partial t}\right|_x + \boldsymbol{u}\nabla \cdot \hat{\boldsymbol{u}}\right)\mathrm{d}\Omega. \tag{27}$$

By use of expression (27) and the traction-free outflow boundary condition (19), the weak formulation of the momentum equations (17) can be written

$$\begin{aligned}\frac{\mathrm{d}}{\mathrm{d}t}\int_{\Omega_t} \boldsymbol{u} \cdot \boldsymbol{v}\mathrm{d}\Omega - \int_{\omega_t} (\boldsymbol{u}\nabla \cdot \hat{\boldsymbol{u}}) \cdot \boldsymbol{v}\mathrm{d}\Omega + \int_{\Omega_t} (\boldsymbol{c} \cdot \nabla \boldsymbol{u}) \cdot \boldsymbol{v}\mathrm{d}\Omega + \\ \frac{1}{\mathrm{Re}}\int_{\Omega_t} \nabla \boldsymbol{u} \,:\, \nabla \boldsymbol{v}\mathrm{d}\Omega - \int_{\Omega_t} p\nabla \cdot \boldsymbol{v}\mathrm{d}\Omega = 0.\end{aligned} \tag{28}$$

The weak form of the Navier-Stokes equations (28) and (18) is approximated on finite-dimensional subspaces that are spanned by the basis functions $\{\phi_i\}_{i=1,\ldots,N_u}$ and $\{\psi_i\}_{i=1,\ldots,N_p}$. The velocity and the pressure are expressed as linear combinations, *viz.*

$$\boldsymbol{u}_h = \boldsymbol{u}_b + \sum_{i=1}^{N_u} \boldsymbol{u}_i \phi_i, \qquad p_h = \sum_{i=1}^{N_p} p_i \psi_i, \tag{29}$$

where $\boldsymbol{u}_b$ satisfies the Dirichlet boundary condition on Γ_u. Due to the highly convective flow in the ascending aorta, the numerical scheme requires a stabilization technique in order to avoid oscillations in the numerical solution. In this study the streamline upwind Petrov-Galerkin method [28] is applied that preserves the consistency of the scheme. The method uses modified velocity-dependent test functions in the weak formulation

$$\tilde{\phi}_i = \phi_i + \tilde{k}_{\mathrm{SUPG}} \frac{\boldsymbol{u} \cdot \nabla \phi_i}{||\boldsymbol{u}||^2}, \quad i = 1, \ldots, N_u, \tag{30}$$

where ϕ_i are the Galerkin test functions and $\tilde{k}_{\mathrm{SUPG}}$ denotes the upwind parameter that controls the factor of upwind weighting. Using the modified functions $\tilde{\phi}_i$ and the basis functions ψ_i as test functions the (upwind modified) Galerkin system can be written in matrix notation

$$\begin{aligned}\boldsymbol{M}\dot{\boldsymbol{u}}_h - \boldsymbol{M}_1\boldsymbol{u}_h + \boldsymbol{K}(\boldsymbol{c}_h)\boldsymbol{u}_h + \boldsymbol{L}\boldsymbol{u}_h - \boldsymbol{Q}^T\boldsymbol{p}_h &= \boldsymbol{f}_h, \\ \boldsymbol{Q}\boldsymbol{u}_h &= 0,\end{aligned} \tag{31}$$

where the prescribed velocities on Γ_u are included on the right-hand-side vector $\boldsymbol{f}$. Herein $\dot{\boldsymbol{u}}$ denotes the fluid acceleration, $\boldsymbol{M}$ is the mass matrix, $\boldsymbol{K}$ the convection matrix, $\boldsymbol{L}$ the diffusion

matrix, $\boldsymbol{Q}^T$ the gradient matrix and $\boldsymbol{Q}$ the divergence matrix. The matrix $\boldsymbol{M}_1$ results from the application of the Reynolds transport theorem and is a mass contribution scaled by the divergence of the domain velocity.

The solution of system (31) requires considerable computational effort. For this reason a so-called projection scheme is applied in this study [29, 30]. It is based on the Helmholtz decomposition principle, which states that any sufficiently regular vector function can be split into a divergence free and a rotation-free vector field. In [31, Chapter 6] it was shown that this decomposition can be applied to the weak formulation of the Navier-Stokes equations in appropriate spaces. The technique splits the problem (31) in the sequence of an advection-diffusion problem for an auxiliary non-divergence-free velocity field and a projection of the intermediate velocity field onto the divergence-free functional space. This method was originally proposed in [32] and [33]. Using Euler backward differences for the time derivative and a Picard iteration scheme on every time step for the linearization of the convective term, the algorithm on time step t^{n+1} reads:

1. In a Burgers step calculate an intermediate velocity field $\tilde{\boldsymbol{u}}^{n+1,m+1}$ from the linearized system

$$\begin{aligned}(\boldsymbol{M} - \Delta t\,\boldsymbol{M}_1 + \Delta t\,\boldsymbol{K}(\boldsymbol{c}^{n+1,m}) + \Delta t\,\boldsymbol{L})\tilde{\boldsymbol{u}}^{n+1,m+1} = \\ \boldsymbol{M}\boldsymbol{u}^{n,m} + \Delta t\,\boldsymbol{Q}^T p^{n+1,m} + \Delta t\,\boldsymbol{f}^{n+1}\end{aligned} \tag{32}$$

   where $\Delta t = t^{n+1} - t^n$ is the time step and $\tilde{\boldsymbol{u}}^{n+1,m+1}$ contains the unspecified node values at the new time level t^{n+1} ($n = 0, \ldots, N-1$) at the iteration step $m+1$ ($m = 0, \ldots, M-1$);
2. Calculate the pressure correction $q^{n+1,m+1}$

$$\bar{\boldsymbol{Q}}\boldsymbol{M}_d^{-1}\bar{\boldsymbol{Q}}^T q^{n+1,m+1} = -\frac{1}{\Delta t}\boldsymbol{Q}\tilde{\boldsymbol{u}}^{n+1,m+1}; \tag{33}$$

3. Calculate the divergence-free velocity field $\boldsymbol{u}^{n+1,m+1}$

$$\boldsymbol{u}^{n+1,m+1} = \tilde{\boldsymbol{u}}^{n+1,m+1} + \Delta t\,\boldsymbol{M}_d^{-1}\bar{\boldsymbol{Q}}^T q^{n+1,m+1}; \tag{34}$$

4 Update the pressure $p^{n+1,m+1}$

$$p^{n+1,m+1} = p^{n+1,m} + q^{n+1,m+1}. \tag{35}$$

In Equations (33) and (34) the symbol $\boldsymbol{M}_d$ stands for the concentrated mass matrix and $\bar{\boldsymbol{Q}}$ and $\bar{\boldsymbol{Q}}^T$ are the modified divergence and gradient matrix with respect to the velocity boundary conditions, where only the normal component of the velocity is considered, The validation of this scheme has been performed in various calculations [34–36],

The calculations use a temporal discretization of about 350 nonconstant time steps per pulse cycle where the minimum step size is $2{\cdot}5 \times 10^{-4}$ s during systolic acceleration and deceleration, The spatial discretization of the flow domain employs eight-node isoparametric brick elements with tri-linear velocity interpolants and constant pressure (325,760 nodes and 316,992 elements leading to a total degree of freedom of 1,294,272), The resulting systems of linear equations are characterized by non-symmetric, ill-conditioned, sparse and large band matrices, They are solved by means of a modified bi-conjugate-gradient algorithm [37] using incomplete LU-/Cholesky-factorization as preconditioning technique, The solution of

the symmetric and positive-definite pressure equation applies the preconditioned conjugate-gradient method. The application of this iterative solution method, together with a compact matrix storage scheme allows the realization of the flow studies on current workstations.

5. Results and discussion

Numerical results of the velocity patterns and wall-shear-stress distributions occurring in the ascending aorta are presented for the healthy configuration and downstream of the artificial heart valve. Blood is modeled as a Newtonian fluid with a constant density of $\rho = 1044$ kg/m^3 and constant viscosity of $\mu = 3{\cdot}65 \times 10^{-3}$ Pa s.

5.1. NATIVE VALVE

The healthy configuration has a mean inflow diameter used as reference length $L_0 = 2{\cdot}71 \times 10^{-2}$ m and a mean inflow velocity $U_0 = 1{\cdot}32 \times 10^{-1}$ m/s resulting in the mean Reynolds number of Re $= 1024$. The Womersley number is $\alpha = 19{\cdot}72$ ($\alpha = L_0\sqrt{\omega/\nu}/2$) where $\omega = 7{\cdot}34$ s^{-1} is the angular frequency corresponding to about 70 heart beats per minute.

To present the predicted velocities in the vessel segment, axial velocity profiles are demonstrated at six planes along the longitudinal direction at three different phase angles during the cardiac cycle (Figure 4). Plane A corresponds to the computational inlet where the MRI-measured and smoothed axial and secondary velocities were used as inflow boundary conditions.

As the flow is highly convective, the development of the boundary layer is confined to a narrow region at the wall. During systolic acceleration until systolic peak is reached, the flow is characterized by essentially flat velocity profiles in the whole segment. A noticeable skewing of the profiles towards the inner wall of the aortic arch can be observed. During flow deceleration flow patterns differ significantly from those during acceleration: zones of reversed flow develop at the inner wall at the entrance to the aortic arch leading to C-shaped profiles with highest velocities at the posterior and outer wall.

In order to validate the velocity predictions gained by the fluid-dynamic calculations, an additional MRI measurement of the three-directional velocity field was performed at plane F. In general, the comparison between the computational results and the MRI data demonstrates good qualitative correspondence, although this is restricted to the systolic phase where higher velocities occur. In Figure 5 contours of the axial velocity component are shown during deceleration. Even though the CFD prediction exhibits larger recirculation and a less pronounced C-shape, the agreement of the patterns is obvious. The same applies for the secondary motion. For high velocities during the systolic phase MRI measurements are of good quality and, thus, the computational results agree very well. Figure 6 shows the velocity streamlines at crosssection F at one specific phase angle during the deceleration phase.

Both the MRI measurements and the CFD result demonstrate two major vortices at the inner wall and the posterior wall, respectively. A very important hemodynamic quantity that cannot be measured directly by MRI is the wall shear stress [38]. Contour plots of the axial WSS distribution during systolic acceleration and systolic deceleration are shown in Figure 7. High stresses occur at the inner wall when the flow is accelerating with the velocity profiles skewed towards this wall. This pattern changes immediately after the systolic peak. A zone of recirculation develops at the inner wall and high stresses migrate along the posterior wall

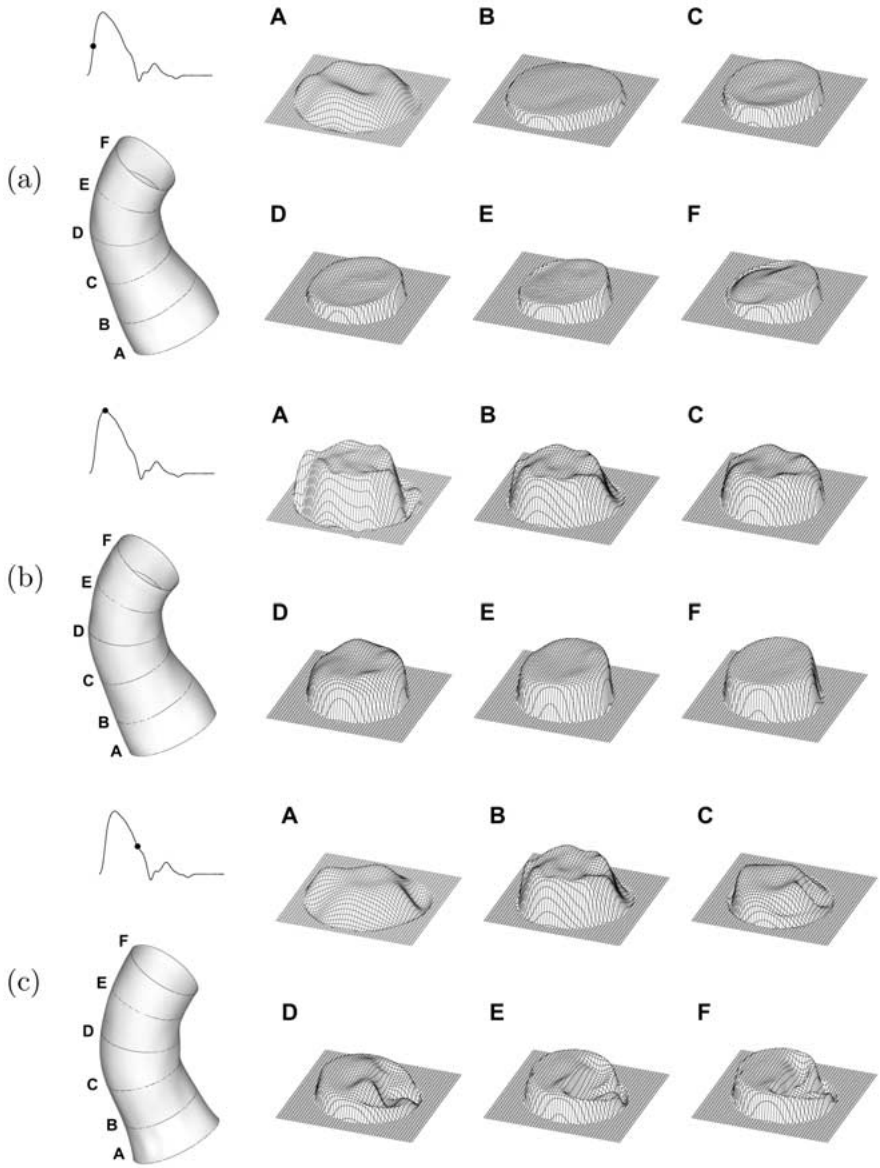

Figure 4. Healthy configuration: axial velocity profiles during systolic acceleration (a) systolic peak (b) and systolic deceleration (c) at cross-sections as indicated.

towards the outer wall. As deceleration continues, zones of low and negative WSS spread over large regions at the inner and anterior wall.

The time history of the WSS is demonstrated at four points located at the anterior, inner, posterior and outer wall at cross-section F (Figure 8). Highest values occur at the inner point and the posterior point during flow acceleration. Even before the systolic peak is reached, the WSS decreases rapidly towards zero at the inner point, while the other three points exhibit moderate values during systolic deceleration. At end diastole the outer point experiences relatively large negative WSS indicating reverse flow at the outer wall at this time.

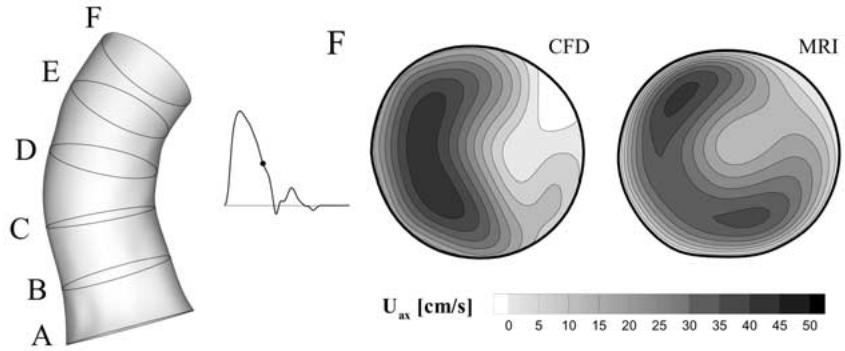

Figure 5. Healthy configuration: axial velocity profiles at cross-section F during systolic deceleration; comparison between CFD result and MRI measurement.

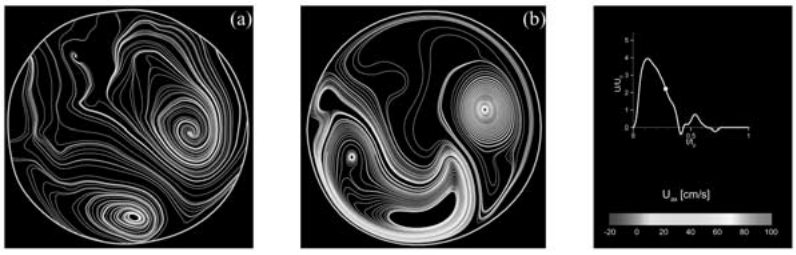

Figure 6. Healthy configuration: streamlines at cross-section F during systolic deceleration color-coded with the velocity magnitude; comparison between MRI measurement (a) and CFD result (b).

5.2. ARTIFICIAL VALVE

For the study of aortic blood flow distal to an artificial heart valve a patient with similar flow parameters, *i.e.*, Reynolds number Re = 948 and Womersley number $\alpha = 18{\cdot}71$, was selected. The underlying physiological parameters are as follows: the inflow diameter $L_0 = 2{\cdot}54 \times 10^{-2}$ m, the mean inflow velocity $U_0 = 1{\cdot}31 \times 10^{-1}$ m/s and the pulse period $T = 0{\cdot}85$ s. Only the axial component of the inflow velocity was measured and incorporated into the calculation. Therefore the contribution of the in-plane velocities could not be considered which constitutes a certain drawback for the comparison with the native configuration.

In Figure 3b the axial velocity profiles just downstream of the artificial valve at systolic peak flow are shown. Two significant jets are expelled from the heart and regurgitation occurs simultaneously at the anterior and posterior wall caused by the specific shape of the implanted artificial valve (shown in Figure 3 on the right-hand side). Corresponding to Figure 4 for the native flow the predicted axial velocity profiles are shown in Figure 9. During systolic acceleration the flow characteristic downstream of the artificial heart valve is very similar to that of the native valve. Due to the high acceleration, blunted profiles develop very quickly. The specific shape of the inflow profiles changes immediately downstream of the valve and a skewing towards the inner wall of the aortic arch can be observed. When acceleration decreases, the inflow profiles are conserved much longer. At the systolic peak the two jets corresponding to the major orifices of the valve prosthesis can still be observed in the aortic arch with a skewing to the posterior wall. At flow deceleration C-shaped profiles arise at the entrance to the aortic arch.

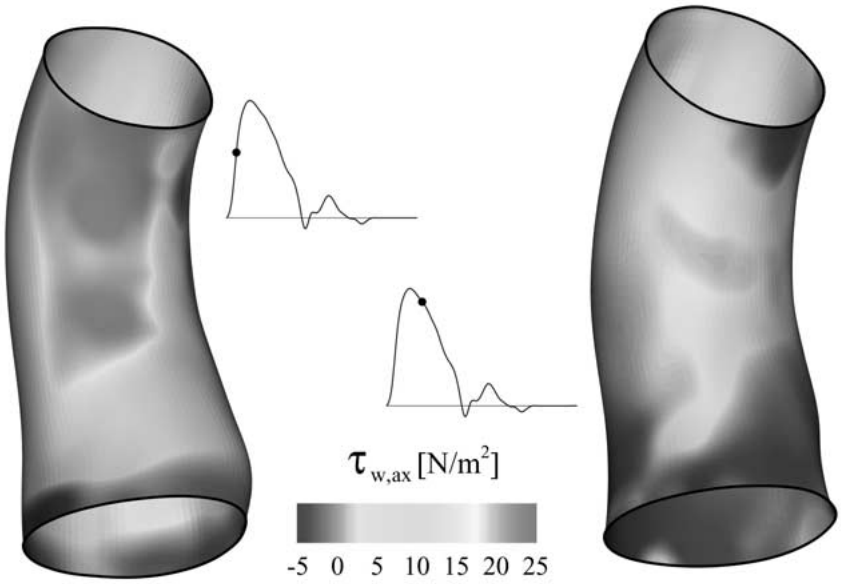

Figure 7. Healthy configuration: axial wall shear stress distribution during systolic acceleration (left) and at the beginning of systolic deceleration (right).

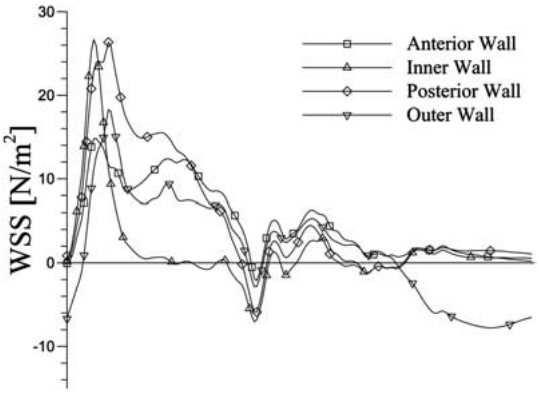

Figure 8. Healthy configuration: axial wall shear stresses at four points at cross-section F over the cardiac cycle (for definition see Figure 2).

The WSS distribution is characterized by significantly higher values than in the healthy configuration (Figure 10). This is primarily caused by the specific flow wave form in this patient: flow acceleration is higher, the flow rate at the systolic peak is about 1·2 times higher and the systolic phase is shorter compared to the volunteer's wave form. Moreover, the two jets that are expelled from the heart become skewed towards the vessel walls, which results in higher WSS at these sites. At the inner wall and at the outer wall downstream of the flow entrance, regions of high WSS develop that persist during the entire systolic phase. During acceleration only a small zone of negative WSS occurs at the flow inlet indicating regurgitation into the heart. During deceleration reversed flow can be observed on large parts of the anterior, inner and outer wall. In Figure 11 the time history of the axial WSS is shown at four points in plane F. The locations correspond to those of the healthy configuration shown in Figure 8. For all four points remarkable oscillations occur during the entire cardiac cycle

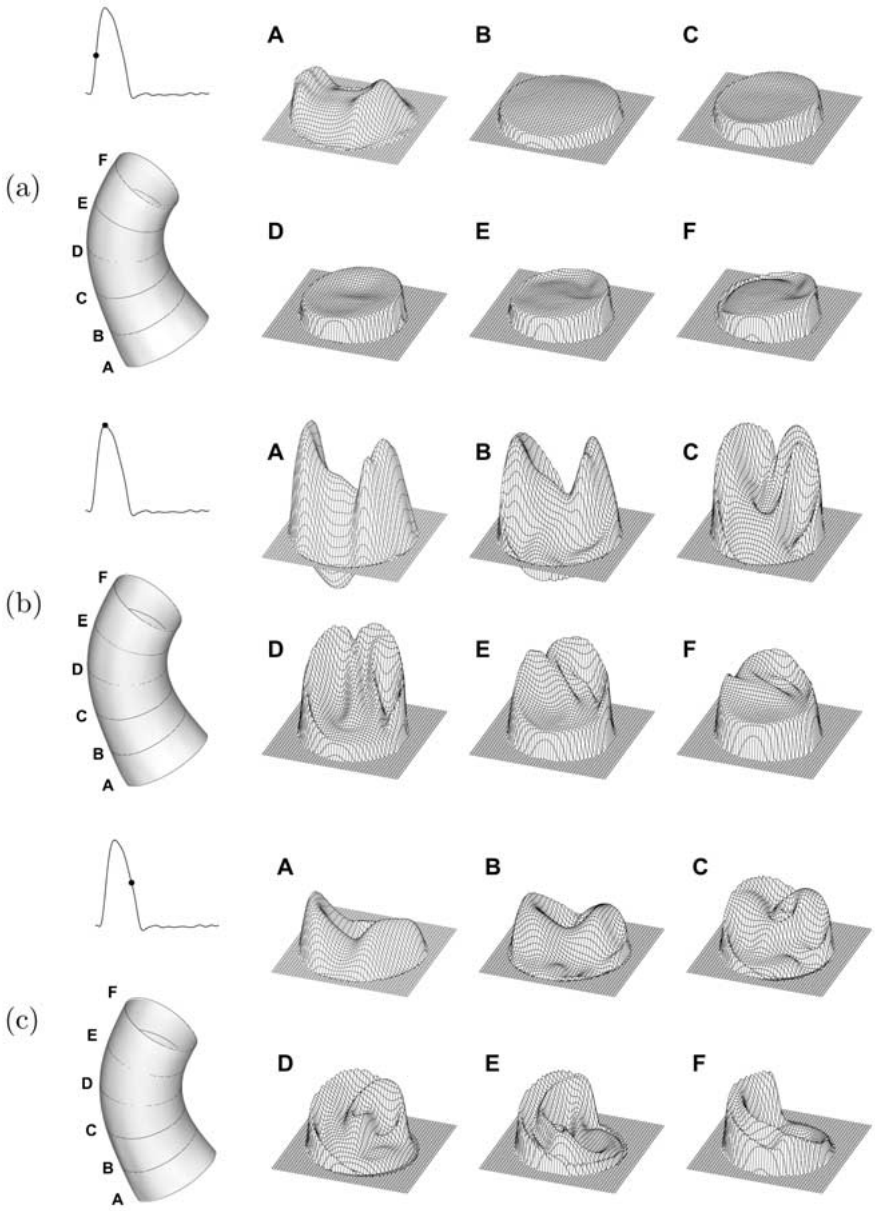

Figure 9. Artificial valve configuration: axial velocity profiles during systolic acceleration (a), systolic peak (b) and systolic deceleration (c) at cross-sections as indicated.

and especially during systole. The posterior point experiences the highest values that are in the range of the ones appearing for the native flow (about 26 N/m^2). At the same location also the lowest stresses can be observed at the beginning of the diastolic phase. As for the healthy configuration approximately at mid-diastole flow reversion develops at the outer wall as indicated by the negative stress values for the outer wall point.

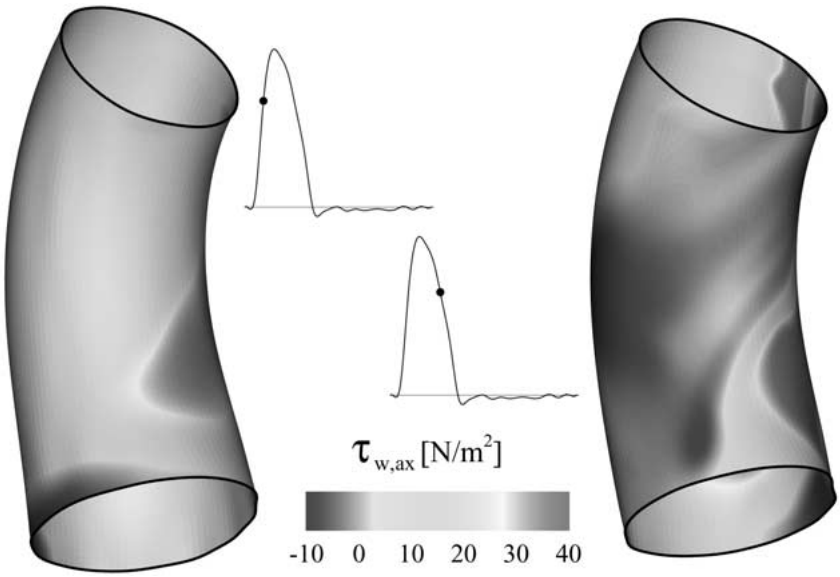

Figure 10. Artificial valve configuration: axial wall-shear-stress distribution during systolic acceleration (left) and systolic deceleration (right).

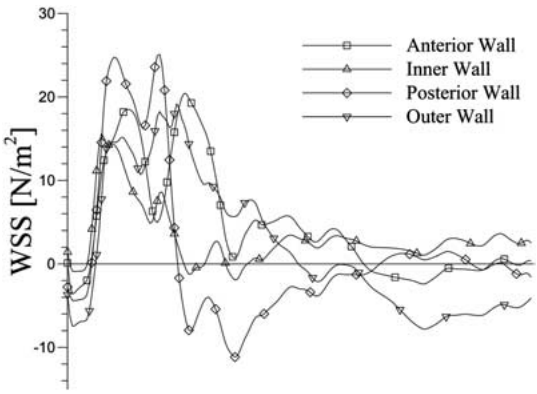

Figure 11. Artificial valve configuration: axial wall shear stresses at four points at cross-section F over the cardiac cycle (for definition see Figure 2).

6. Conclusion

A new approach for studying details of human blood flow based on computational simulations in realistic, time-varying anatomic models as obtained from MRI data has been presented. Integration of moving slice acquisition into the MRI protocol, as well as dedicated methods for CFD, such as the ALE-modified Navier-Stokes solver for three-dimensional, time-dependent Newtonian fluid flow in moving geometries, resulted in realistic simulations. The comparison of flow patterns predicted from simulations with data measured by MRI indicate the validity of the methods suggested. A first application assessing differences of blood flow and wall shear stress of native and mechanical valves illustrate the potential for detailed studies of blood flow in and around cardiovascular implants *in vivo*. As such the combination of CFD and MRI appears to be a promising tool for studying designs of implants helping to further improve their *in vivo* performance.

Acknowledgements

This study is supported by the Austrian Science Foundation, Project-No. P 14 321-TEC, Vienna, Austria, and by EUREKA Project No. E!2061.

References

1. K.B. Chandran, Flow dynamics in the human aorta. *J. Biomech. Engng.* 115 (1993) 611–616.
2. R.M. Nerem, Hot-film measurements of arterial blood flow and observations of flow disturbances. In: N.H.C. Hwang and N.A. Norman (eds.), *Cardiovascular Flow Dynamics and Measurements*. Baltimore/London/Tokyo: University Park Press (1977) pp. 191–215.
3. M.H. Friedman. Geometric risk factors for arteriosclerosis. *Arteriosclerosis* 4 (1983) 85–94.
4. S.A. Berger, L. Talbot and L.S. Yao, Flow in curved tubes. *Ann. Rev. Fluid Mech.* 15 (1983) 461–512.
5. K. Ohba, H. Kamino, T. Urabe and S. Ikedo, Pulsatile flow through a tapered U-bend as simulated aortic arch (flow characteristics and velocity field). In: R.A. Gerbsch and K. Ohba (eds.), *Proc. ASME FED Symposium on BioMedical Fluids Engineering*, volume 212. Hilton Head, South Carolina (1995) pp. 23–28.
6. S. Jin, J. Oshinski and D. Giddens, Effects of inflow conditions and wall motion on flow in the ascending aorta. In: R.D. Kamm, G.W. Schmid-Schönbein, G.A. Ateshian, and M.S. Hefzy (eds), *Proc. 2001 Bioengineering Conference*, volume BED-Vol. 50. New York: ASME (2001) pp. 13–14.
7. D. Mori and T. Yamaguchi, Computational fluid dynamics modeling and analysis of the 3-d distortion of the human aortic arch. *Comput. Meth. Biomech. Biomed. Engng.* 5 (2002) 249–260.
8. A. Leuprecht, K. Perktold, S. Kozerke and P. Boesiger, Combined CFD and MRI study of blood flow in a human ascending aorta model. *Biorheology* 39 (2002) 425–429.
9. S.J. Weston, N.D. Wood, G. Tabor, A.D. Gosman and D.N. Firmin, Combined MRI and CFD analysis of fully developed steady and pulsatile laminar flow through a bend. *J. Magn. Reson. Imag.* 8 (1998) 1158–1171.
10. J.A. Moore, D.A. Steinman, D.W. Holdsworth and C.R. Ethier, Accuracy of computational hemodynamics in complex arterial geometries reconstructed from magnetic resonance imaging. *Ann. Biomed. Engng.* 27 (1999) 32–41.
11. Q. Long, X.Y. Xu, M. Bourne and T.M. Griffith, Numerical study of blood in an anatomically realistic aorto-iliac bifurcation generated from MRI data. *Magn. Reson. Med.* 43 (2000) 565–576.
12. F.P. Glor, J.J.M. Westenberg, J. Vierendeels, M. Danilouchkine and P. Verdonck, Validation of the coupling of magnetic resonance imaging velocity measurements with computational fluid dynamics in a U bend. *Artificial Organs* 26 (2002) 622–635.
13. Y.R. Woo and A.A. Yoganathan, In vitro pulsatile flow velocity and turbulent shear stress measurements in the vicinity of mechanical aortic heart valve prostheses. *Life Support Syst.* 3 (1985) 283–312.
14. J.M. Hasenkam, E.M. Pedersen, J.H. Ostergaard, H. Nygaard, P.K. Paulsen, G. Johannsen and B.A. Schurizek, Velocity fields and turbulent stresses downstream of biological and mechanical aortic valve prostheses implanted in pigs. *Cardiovasc. Res.* 22 (1988) 472–483.
15. M. Giersiepen, L.J. Wurzinger, R. Opitz and H. Reul, Estimation of shear stress-related blood damage in heart valve prostheses – *in vitro* comparison of 25 aortic valves. *Int. J. Artif. Organs* 13 (1990) 300–306.
16. T.J.R. Hughes, W.K. Liu and T.K. Zimmermann, Lagrangian-Eulerian finite element formulation in incompressible viscous flows. *Comput. Methods Appl. Mech. Engng.* 29 (1981) 329–349.
17. K. Boukir, B. Nitrosso and B. Maury, A characteristics-ALE method for variable domain Navier-Stokes equations. In: L.C. Wrobel, B. Sarler, and C.A. Brebbia (eds.), *Computational Modelling of Free and Moving Boundary Problems III*. Southampton/Boston: Comput. Mech. Publ. (1995) pp. 57–65.
18. A. Quarteroni and L. Formaggia, Mathematical modelling and numerical simulation of the cardiovascular system. MOX-Report No. 01 (2002).
19. S. Kozerke, J.M. Hasenkam, H. Nygaard, P.K. Paulsen, E.M. Pedersen and P. Boesiger, Heart motion-adapted MR velocity mapping of blood velocity distribution downstream of aortic valve prostheses: initial experience. *Radiology* 218 (2001) 548–555.
20. S. Kozerke, M.B. Scheidegger, E.M. Pedersen and P. Boesiger, Heart motion adapted cine phase-contrast flow measurements through the aortic valve. *Magn. Reson. Med.* 42 (1999) 970–978.
21. P. Dierckx. *Curve and Surface Fitting with Splines*. Oxford/New York/Tokyo: Clarendon Press (1993), 285 pp.

22. C. Reinsch, Smoothing by spline functions. *Numerische Mathematik* 10 (1967) 177–183.
23. J. Donea, Arbitrary Lagrangian Eulerian finite element methods. In: T. Belytschko and T. Hughes (eds.), *Computational Methods for Transient Analysis*. Volume 1 of *Computational Methods in Mechanics*. Amsterdam: North-Holland, Elsevier (1983) pp. 474–515.
24. A. Quarteroni, M. Tuveri, and A. Veneziani, Computational vascular fluid dynamics. Problems, models and methods. *Comput. Visualisation Sci.* 2 (2000) 163–197.
25. L. Formaggia and F. Nobile, A stability analysis for the arbitrary Lagrangian Eulerian formulation with finite elements. *East West J. Num. Math.* 7 (1999) 105–131.
26. R. Aris, *Vectors, Tensors, and the Basic Equations of Fluid Mechanics*. Englewood Cliffs, N.J.: Prentice Hall (1962) 286 pp.
27. L.E. Malvern, *Introduction to the Mechanics of a Continuum Medium*. Englewood Cliffs, N.J.: Prentice Hall (1969) 713 pp.
28. A.N. Brooks and T.J.R. Hughes, Streamline upwind/Petrov Galerkin formulations for convection dominated flows with particular emphasis on incompressible Navier-Stokes equations. *Comput. Meth. Appl. Mech. Engng.* 32 (1982) 199–259.
29. K. Perktold and G. Rappitsch, Mathematical modeling of local arterial flow and vessel mechanics. In: J. Crolet and R. Ohayon (eds.), *Computational Methods for Fluid Structure Interaction*, New York: Wiley (1994) pp. 230–245.
30. K. Perktold and G. Karner, Computational principles and models of hemodynamics. In: M. Hennerici and S. Meairs (eds.), *Cerebrovascular Ultrasound Theory, Practice and Future Developments*. Cambridge University Press (2001) pp. 63–76.
31. V. Girault and P.-A. Raviart, *Finite Element Methods for Navier-Stokes Equations*. Berlin/Heidelberg/New York/Tokyo: Springer (1986) 374 pp.
32. A.J. Chorin, Numerical solution of the Navier Stokes Equations. *Math. Comput.* 22 (1968) 745–762.
33. R. Temam, Sur l'approximation de la solution des équations de Navier-Stokes par la méthode de pas fractionnaires (II). *Arch. Rat. Mech. Anal.* 33 (1969) 377–385.
34. K. Perktold, On numerical simulation of three-dimensional physiological flow problems. *Ber. Math.-Stat. Sektion, Forschungsgesellschaft Joanneum Graz.* (Nr. 280/5) (1987).
35. K. Perktold, M. Resch, and H. Florian, Pulsatile non-Newtonian flow characteristics in a three-dimensional human carotid artery bifurcation model. *Trans ASME J. Biomech. Engng.* 113 (1991) 464–475.
36. G. Karner, K. Perktold, M. Hofer and D. Liepsch, Flow characteristics in an anatomically realistic compliant carotid artery bifurcation model. *Comput. Meth. Biomech. Biomed. Engng.* 2 (1999) 171–185.
37. M. Hofer and K. Perktold, Vorkonditionierter konjugierter Gradienten Algorithmus für große schlecht konditionierte unsymmetrische Gleichungssysteme. Supplement Volume *Z. angew. Math. Mech.* 75 SII (1995) 641–642.
38. D.N. Ku, D.P. Giddens, C.K. Zarins and S. Glagov, Pulsatile flow and atherosclerosis in the human carotid bifurcation. Positive correlation between plaque location and low oscillating shear stress. *Arteriosclerosis* 5 (1985) 293–302.